Ground-Based Polarimetric SAR Interferometry for the Monitoring of Terrain Displacement Phenomena–Part I: Theoretical Description

Rubén Iglesias, *Student Member, IEEE*, Albert Aguasca, *Member, IEEE*, Xavier Fabregas, *Member, IEEE*,
Jordi J. Mallorqui, *Senior Member, IEEE*, Dani Monells, *Student Member, IEEE*,
Carlos López-Martínez, *Senior Member, IEEE*, and Luca Pipia

Abstract—Ground-based synthetic aperture radar (SAR) (GB-SAR) sensors represent an effective solution for the monitoring of ground displacement episodes. Initially, the most GB-SAR sensors were based on vector network analyzers (VNA). This type of solution, characterized by a slow scanning time comparable to the decorrelation of the troposphere medium, compromised in many cases the quality of final products for the application of persistent scatterer interferomerty (PSI) techniques. The development of GB-SAR sensors based on the use of stepped linear frequency modulated continuous wave (SLFMCW) signals has led to significant improvements during the last years. They have allowed fulfilling the need of temporal homogeneity of the troposphere during the acquisition time and, moreover, they have favored the acquisition of reliable polarimetric SAR (PolSAR) measurements without drastically increasing the scanning time. This fact has boosted the inclusion of polarimetric SAR interferometry (PolInSAR) algorithms in PSI processing chains, which are demonstrating to outperform classical single-polarimetric performances. The objective of this paper is twofold. On the one hand, a general overview of the polarimetric RiskSAR sensor, developed by the Universitat Politècnica de Catalunya (UPC), is put forward as an example of SLFMCW GB-SAR system implementation. On the other hand, a complete theoretical description of ground-based SAR (GB-SAR) interferometry (GB-InSAR) techniques for PSI purposes is widely discussed. The adaptation of the Coherent Pixels Technique to obtain the linear and nonlinear components of ground displacement phenomena is proposed. In the second part of this paper, the displacement maps and time series over two very different scenarios are presented in order to show the feasibility of GB-SAR sensors for terrain displacement monitoring applications.

Index Terms—Differential synthetic aperture radar (SAR) interferometry (DInSAR), frequency modulated continuous wave (FMCW) radar, GB-SAR interferometry (GB-InSAR), ground-based SAR (GB-SAR), persistent scatterer interferomerty (PSI), polarimetric SAR interferometry (PolInSAR), stepped linear FMCW (SLFMCW) radar.

I. INTRODUCTION

DATA COLLECTED by spaceborne synthetic aperture radar (SAR) sensors allow obtaining all-weather terrain complex reflectivity images, which can be processed by means of differential SAR interferometry (DInSAR) algorithms for the monitoring of complex deformation episodes [1], [2] with millimetric accuracy [3]. DInSAR techniques are based on exploiting the phase-differences, i.e., the interferogram, between multitemporal pairs of single look complex (SLC) SAR acquisitions of the same area of study, to obtain the terrain displacement undergone in the line-of-sight (LOS) direction. This technique has led to the development of persistent scatterer interferomerty (PSI) [4]–[15], in which large multitemporal data sets are employed in order to generate multiple phase relationships between the SAR acquisitions available. PSI techniques allow the estimation of both the linear and the nonlinear component of terrain displacements, as well as the atmospheric phase screen (APS) for each acquisition.

During the last decade, PSI techniques applied over spaceborne data have proven to be a useful solution to carry out the geophysical interpretation of several subsidence phenomena, especially when large scale areas of observation are required. Contrarily, when high flexibility in terms of revisiting-time is required or the sensor orientation needs to be fitted to the specific characteristics of the area under study, spaceborne solutions present several limitations, which compromise the applicability of PSI techniques.

In order to overcome these limitations, the research activity of several groups has been addressed to the development of ground-based SAR (GB-SAR) sensors. Easy to deploy and cheaper if compared with spaceborne solutions, GB-SAR sensors are a potential alternative ideal for the monitoring of small-scale areas. The high stability of the sensor platform and its flexibility in terms of revisiting-time make these systems an excellent option to detect small changes within the area of interest with a high temporal resolution of up to few minutes or even seconds. Moreover, the chances to fit the illumination angle to maximize the detection of LOS displacements allow overcoming the intrinsic limitations of spaceborne solutions which are constrained by the orbit geometry.

The first paper about GB-SAR inferometry (GB-InSAR) date from 1999 [16], [17]. For the first time, the potentials of terrestrial SAR sensors in the field of civil engineering

This article has been accepted for inclusion in a future issue of this journal. Content is final as presented, with the exception of pagination.

2   IEEE JOURNAL OF SELECTED TOPICS IN APPLIED EARTH OBSERVATIONS AND REMOTE SENSING

were demonstrated studying the displacements of a dam. The equipment employed at that time consisted of a radar-based on a vector network analyzer (VNA) architecture, a coherent transmitting–receiving setup, a mechanical guide and a PC to control the data acquisition process. Some years later, in 2003, the company Ellegi-LiSALab obtained a license to exploit this technology from Joint Research Center (JCR). This first system intended for commercial exploitation was called linear SAR (LiSA). At this time, VNA solutions based on the linear frequency sweeping of transmitted signals presented a high flexibility in the generation of tones and the opportunity to assemble GB-SAR systems with simple electronic hardware. Advanced versions based on this setup followed with the objective of improving the stability and bandwidth capabilities of GB-SAR sensors [18]–[26]. Among all these sensors, the IBIS-L/M provided by the Italian company Ingegneria Dei Sistemi (IDS) has demonstrated to be a powerful and versatile steepest frequency continuous wave (SFCW) radar, which has shown its usefulness in a large number of applications [27]–[31]. Today, it is considered the most popular commercial GB-SAR sensor.

Despite the popularity reached by VNA-based GB-SAR solutions, during the last decade, this radar architecture is being replaced by specifically developed prototypes based on the use of high rate steepest linear frequency modulated continuous wave (SLFMCW) signals [32]. In contrast to VNA-based solutions, SLFMCW GB-SAR sensors are able to perform faster scans, reducing the scanning one order of magnitude (from 10 to 1 min). This has allowed not only to minimize the impact of troposphere disturbances but also to reduce the amplitude and phase distortions due to target instabilities during the scanning time. Faster scans have led to significant improvements in GB-InSAR performance for the monitoring of ground displacements with PSI techniques. This is the case of the polarimetric RiskSAR sensor, which is under continuous development at Remote Sensing Laboratory (RSLab) of Universitat Politècnica de Catalunya (UPC) since 2004 [32]–[34].

Finally, new promising prototypes have been proposed in these last few years. On the one hand, the company Gamma Remote Sensing has presented a real aperture radar (RAR) sensor that is demonstrating similar monitoring performances [35] compared with SAR-based solutions. On the other hand, the company MetaSensing has recently introduced the FastGBSAR concept based on applying airborne SLFMCW SAR technology on terrestrial SAR sensors, which allows fast scans up to 4 s [36]. Another example of very fast GB-SAR sensors is the one developed by the Institute for Radiophysics and Electronics from the National Academy of Sciences of Ukraine (NASU), which is based on noise radar technology [37].

This paper is based on describing the last developments in the hardware and in the GB-InSAR processing chain of the polarimetric RiskSAR sensor. The work presented is focused on the sensor working in a discontinuous monitoring mode, i.e., the area of interest is revisited at different measurement days. First, the way of obtaining a time-averaged SLC image from each measurement day is put forward. Then, the different alternatives to compensate the impact of atmospheric artifacts among the different time-averaged acquisitions are widely discussed. This step is mandatory to reduce the impact of the atmospheric artifacts in the displacement map estimations, most noticeable on the deformation time-series. Finally, the adaptation of Coherent Pixels Technique (CPT) [4], [38] to work with zero-baseline GB-SAR data is presented. The way of exploiting the capabilities of polarimetric SAR (PolSAR) data if available is also discussed along the whole processing chain.

The second part of this paper [39] is focused on the practical side of the techniques presented in this paper. Results obtained from RiskSAR data over two different scenarios with different displacement phenomena are presented and deeply discussed, pointing out the key measuring and processing particularities for each case.

This paper is organized as follows. Section II presents a hardware description of the RiskSAR sensor, highlighting the main advantages of the SLFMCW radar philosophy. In Section III, the different operation modes, which constrain the GB-InSAR processing, are briefly reviewed. Sections IV–VI present the whole processing chain for ground displacement monitoring with focus in the discontinuous operation mode. The main conclusion and major remarks of the manuscript are given in Section VII.

II. RISKSAR SENSOR

A. Radar Architecture

The RiskSAR sensor [32]–[34] is a transmitter–receiver instrument that generates an SLFMCW waveform with a digital direct synthesizer (DDS). The continuous wave operation mode significantly simplifies the system architecture with respect to pulsed radars. This radar architecture is based on the use of commercial off-the-shelf (COTS) components in the radio frequency (RF), intermediate frequency (IF), control and data storage sections. The output signal of the DDS is filtered in order to reduce nondesired harmonics and spurious. A first up-conversion to L-band is done by means of a mixer. An active multiplier performs the second and last frequency up-conversion.

Regarding receiver unit, it consists of a low-noise chain with a direct phase quadrature I/Q Zero-IF demodulator, where a sample of the transmitted signal is used as a local oscillator. A high-pass filter is included in the video amplifier, which ensures that the dynamic range of the base-band signal is properly compressed and compensated.

The base-band signal acquisition is performed with a commercial National Instruments (NI) PXI data acquisition (DAQ) device with two 14-bits channels, each with a sampling capacity up to 100 Ms/s and 512 MB memory depth, which is controlled by a computer. The phase and quadrature I/Q base-band signals are synchronously digitized using trigger and clock references that are coherently generated in the frequency generation unit. Fig. 1 shows the block diagram of the RiskSAR sensor.

B. System Description

The polarimetric RiskSAR sensor is able to work at C-, X-, and Ku-bands. It employs a radar system featuring four linearly polarized pyramidal horn antennas for the acquisition of zero-baseline PolSAR collections. The pyramidal shape of
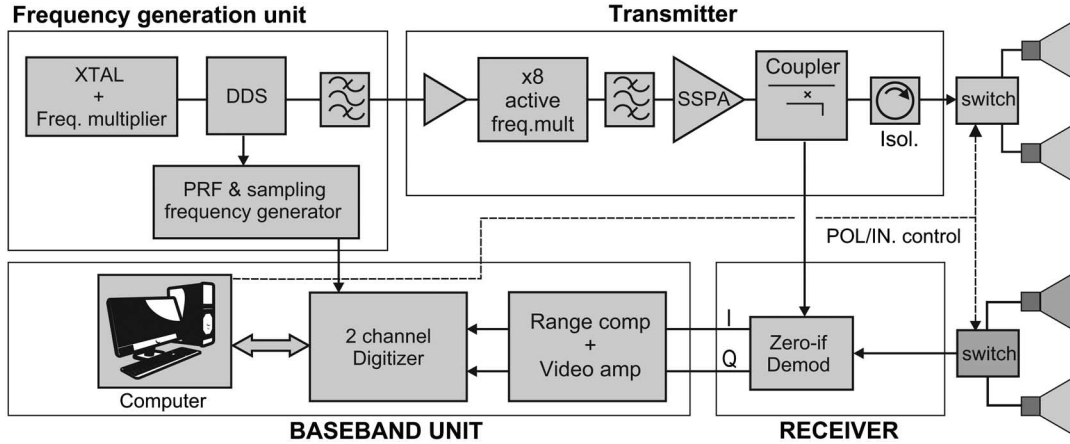
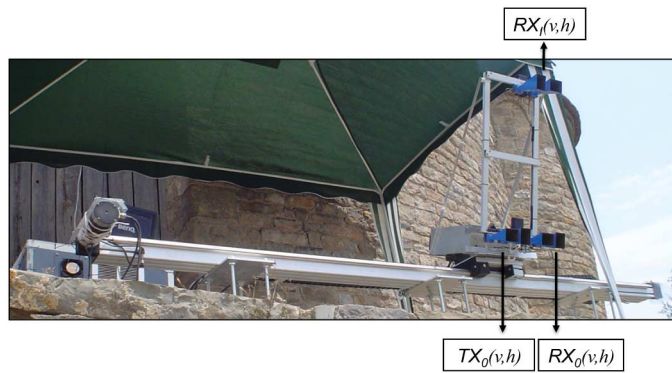Fig. 1. Block diagram of the RiskSAR internal architecture.

Fig. 2. Layout of the X-band horn antennas mounted on the polarimetric interferometric front-end of the RiskSAR system. $TX_0(v, h)$ refers to the horizontal and vertical polarization transmitting antennas, $RX_0(v, h)$ refers to the receiving zero-baseline antennas, and $RX_I(v, h)$ refers to the receiving interferometric antennas.

TABLE I
RISKSAR SETTING PARAMETERS

System parameters	C-band	X-band	Ku-band
Carrier frequency (f_0)	5.3 GHz	9.65 GHz	17.5 GHz
Chirp sampling frequency (f_s)	49.06 MHz	81 MHz	81 MHz
Chirp PRF	20 KHz	20 KHz	20 KHz
Chirp bandwidth	50 MHz	120 MHz	200 MHz
Deramped signal bandwidth	11 MHz	11 MHz	21 MHz
Transmitted power	33 dBm	30 dBm	30 dBm
3 dB antenna beamwidth	32 °	27 °	25 °
Range time-average factor	128	128	128
Synthetic aperture length	2 m	2 m	2 m
Acq. time: sing/full pol	1/2.5 min	1/2.5 min	2/5 min

the antennas allows reaching high directivities with manageable antenna sizes. In addition, this type of antennas fulfills the polarimetric purity requirements needed in PolSAR data applications. In this framework, two horn antennas are used for transmitting in horizontal and vertical polarization $TX_0(v, h)$, and two more for the zero-baseline signal reception $RX_0(v, h)$ (see Fig. 2). PolSAR data are acquired by switching among the selected combinations of transmitting and receiving antennas. Optionally, when nonzero-baseline fully polarimetric interferometric measurements are required, two extra antennas can be mounted $RX_I(v, h)$ (see Fig. 2). The position of these two last horns is not fixed and they should be adapted to the sensitivity required for the interferometric measurement.

The entire radar-and-antennas assembly is mounted on a linear rail of 2 m length. Each scan takes at C- and X-bands approximately 1 min when the sensor is working in single-polarization mode, whereas 2.5 min are required for the acquisition of full-polarization data. At Ku-band, the scanning time increases to 2 min for the acquisition of single-polarization data and 5 min for the full-polarization case. Table I summarizes the main specifications of the system for each band.

RiskSAR measurements are typically carried out at X-band. Working at X-band, the RiskSAR sensor employs a carrier frequency of 9.65 GHz and transmits a bandwidth of 120 MHz. This frequency, which favors working with higher bandwidths with respect to lower bands, provides a good tradeoff to achieve high spatial resolution SLC images and compensable APS during interferograms exploitation. On the one hand, the high-resolution capabilities at X-band give place to a significant improvement in terms of pixels selected with respect to C- or L- bands. The possibility of GB-SAR sensors to reduce the revisiting-time, to carry out even a continuous monitoring, compensates the impact of the major decorrelation phenomena expected at X-band. On the other hand, the effect of APS is lower than the one produced at Ku-band. The range resolution of the RiskSAR sensor working at X-band is 1.25 m.

Finally, as it happens in all GB-SAR systems available, there is a restriction in the cross-range resolution related with the limited length of the aperture. This is translated into a significant degradation of the cross-range resolution compared with either space- or airborne SAR systems. In fact, all GB-SAR sensors behave as RAR, in which the cross-range resolution is not constant along range. Considering a 2-m aperture length the angular cross-range resolution is on the order of 10 milliradians at X-band. This means that resolution ranges from 0.75 m at near range up to roughly 5 m at a far range of 1500 m. A plot of a typical measurement setup used in the RiskSAR campaigns is shown in Fig. 3.
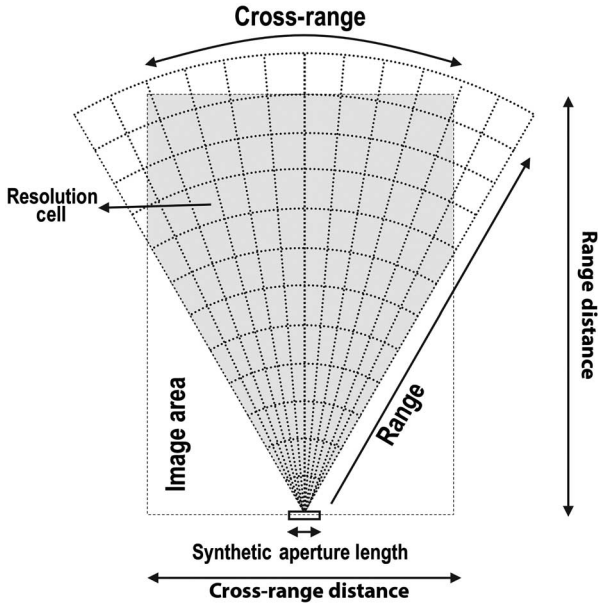
Fig. 3. Sketch of the RiskSAR measurement setup.

III. GB-SAR OPERATIONS MODES

A. GB-SAR Limitations

Once a specific area is selected to be monitored, two different *modus operandi*, referred in the following to as continuous and discontinuous operation modes, shall be considered. This choice will directly impact in the later data processing and may compromise the reliability of the displacement maps estimations.

The continuous operation mode relies on leaving the instrument fixed on the same site during the whole period of measurements, thus performing repetitive and continuous scans of the area of interest. One of the main advantages of employing GB-SAR sensors is that the radar system can remain in the same spatial position in order to keep the same geometrical path between the different acquisitions. When a continuous monitoring is not required and the temporal span between subsequent acquisitions becomes long, the GB-SAR system, including the mechanical frame, may be mounted and dismounted in each measurement campaign. This *modus operandi* is referred to as discontinuous monitoring. In that case, the repositioning of the sensor may be subject to human errors and may introduce geometric decorrelation, which affects the coherence along the multitemporal data set [29]. A careful repositioning strategy, carried out through the use of precise mechanical positioning structures, is mandatory to ensure a millimetric accuracy and avoid the later registration of data. Indeed, the accuracy required in the repositioning is related to the band employed. The larger the carrier frequency the better the accuracy required. It must be pointed out that errors related with bad repositioning are usually nonnegligible, especially when the GB-SAR location is fixed using some marks [29].

The choice of the *modus operandi* typically corresponds to the most efficient and less-costly solution to overcome GB-InSAR limitations. These limitations depend on the characteristics of the area under study and on the dynamics of the deformation process. They may be summarized as follows.

1) GB-InSAR techniques require a dense network of high-quality pixels along the whole period of observation to get reliable results. In this context, temporal decorrelation phenomenon is the main source of phase quality degradation. It is more noticeable over vegetated areas. Decreasing the temporal span between consecutive acquisitions reduces the temporal decorrelation in the interferograms and leads to a more dense network of high-quality scatterers.

2) The second critical limitation corresponds to the aliasing effect due to the phase wrapping inherent to the interferometric phase. Phase differences are characterized by varying between $[-\pi, \pi]$. A temporal displacement undergone may hence be unambiguously estimated when the relative displacement produced between consecutive acquisitions leads to absolute phase differences lower than π radians. At X-band, it corresponds to a relative displacement of roughly 8 mm.

3) Finally, the effect of atmospheric artifacts on measures also plays an important role. Scenarios characterized by having hard atmospheric conditions lead to strong distortions in phase differences along time. Under those conditions, the APS compensation process in presence of large temporal spans is complex, or sometimes impossible to fulfill, leading to significant errors in the final estimated displacement maps.

An adequate operation mode should hence be selected in order to ensure a dense enough coherent pixels network, avoid phase unwrapping ambiguities, and minimize the effect of APS.

B. Continuous Operation Mode

The continuous operation mode is typically employed when fast displacements are expected in order to avoid ambiguous measurements when interferometric phase wraps. In such cases, temporal decorrelation is minimized, especially when working over vegetated areas. Moreover, this operation mode allows GB-SAR sensors to potentially work as an early warning system (EWS) under some special conditions, as seen below. The ability of GB-SAR sensors to perform repetitive and continuous scans makes them an ideal solution to face urban risk of collapse or geohazard mitigation when other strategies, such as orbital-based PSI, are insufficient.

The absolute phase $\varphi_n(t)$ from a nth target, illuminated with a monochromatic wave traveling at the speed of light c, at the frequency f_c, in a certain instant t, is characterized by its own backscattering phase φ_0, by the two-way propagation delay term proportional to the zero-doppler range distance r_n between the target and the sensor, and by a phase contribution referred to as the atmospheric artifacts $\varphi_{n,APS}(t)$

$$\varphi_n(t) = \varphi_0 + \frac{4\pi f_c r_n}{c} + \varphi_{n,APS}(t). \tag{1}$$

Contrarily to the spaceborne case, in which the spatial baseline changes from acquisition to acquisition since the scene is seen from slightly different points of view, the GB-SAR case
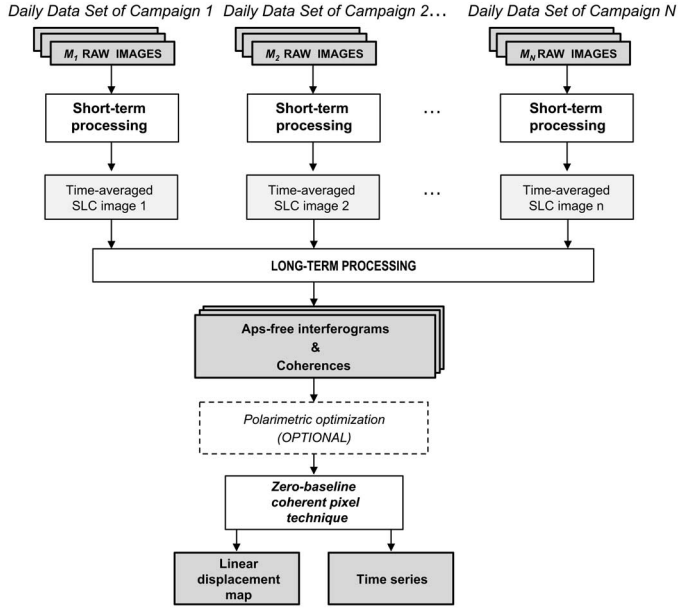
Fig. 4. GB-InSAR-PSI processing considering a discontinuous monitoring formed by N generic measurement days composed by M_i GB-SAR images in each one.
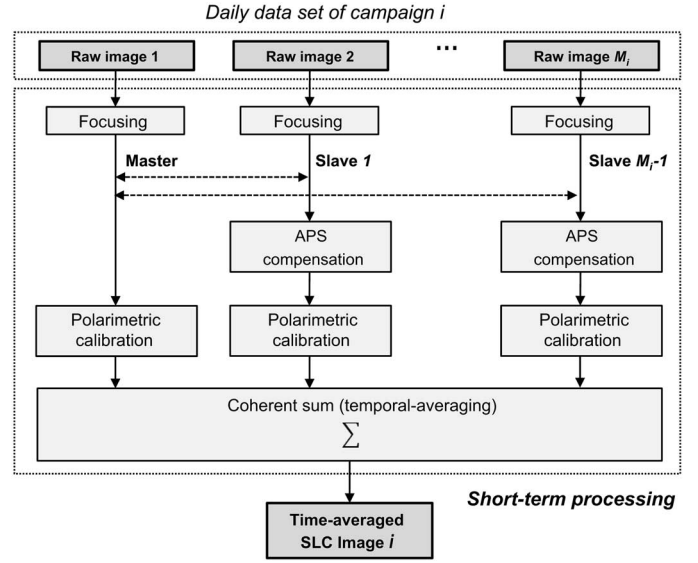

Fig. 5. Short-term processing (STP) chain for the focusing, estimation of the short-term APS artifacts, polarimetric calibration, and temporal averaging of a generic daily data set collection i.

is characterized by acquiring images always from exactly the same position. In such a case, there is not any topographic contribution in the interferometric phase.

When monitoring small-scale phenomena at low-low range distances ($<500\,\mathrm{m}$) under stable APS conditions, the term $\varphi_{n,APS}$ may be neglected. Under these conditions, the interferometric phase $\Delta\varphi_n$ of interferograms can be directly related with the terrain displacement produced between times t_1 and t_2 in the LOS direction

$$\Delta\varphi_n(t_1, t_2) = \varphi_n(t_2) - \varphi_n(t_1) = \frac{4\pi f_c}{c} \cdot \Delta r_n \qquad (2)$$

where Δr_n indicates the physical displacement of the nth target in LOS, thus demonstrating that GB-SAR sensors may potentially work as EWS. The processing required for this case is typically carried out through a direct integration of phase-differences between consecutive acquisitions. When the APS is not negligible, it must be compensated for before carrying out one of the methods proposed in the following section.

Despite the clear advantages of this configuration mode in terms of complexity, it also entails some drawbacks. The most important one is the loss of availability of the instrument since it is intrinsically blocked to its application in a single scenario, with the increase in the cost of operation. For this reason, this *modus operandi* seems clearly inefficient when there is no need to perform a continuous monitoring.

C. Discontinuous Operation Mode

Under the discontinuous operation mode, the GB-SAR sensor is not blocked, allowing a more effective use of the instrument for the simultaneous monitoring of different scenarios. The maintenance cost and the chance of damages of an unattended the system are also drastically reduced. This operation

mode is typically employed for the monitoring of slow-rate displacement phenomena, where a continuous monitoring results clearly inefficient. Nonetheless, the non accomplishment of the hypothesis of negligible atmospheric artifacts, jointly with the larger temporal decorrelation phenomena expected, make the processing chain more complex than before.

Fig. 4 shows the flowchart of the RSLab's GB-InSAR processing chain considering a discontinuous monitoring formed by N generic acquisition dates, composed by M_i images acquired in each one, with $1 \le i \le N$. Each block of this flowchart is discussed in detail hereinafter.

IV. SHORT-TERM PROCESSING

As seen in the previous section, under the discontinuous operation mode the area of interest is revisited along N different measurement days with a certain temporal span. In order to improve the signal-to-noise ratio (SNR) of time-stationary targets, instead of making a single measure, several acquisitions M_i are carried out in each measurement day i. Summarizing, a total of N daily data sets, each one composed by M_i zero-baseline GB-SAR raw images, are available.

The objective of the STP block, see Fig. 5, is to obtain a SNR improved time-averaged SLC image from each daily data set i.

The first step of the STP block consists of focusing the raw images available for each measurement day. This step requires the range and azimuth compression of the data. Since the RiskSAR sensor is based on an SLFMCW radar [32]–[34], the range compression can be performed through a simple FFT of the time-domain deramped received signal. Since the cross-range resolution is not constant due to the limited length of the synthetic aperture, the back-projection technique proved to be the most suitable for the azimuth focusing [40].

Once all the images are focused, and before obtaining the time-averaged SLC image for each daily data set, an appropriate

APS estimation and compensation [18], [41], [42] needs to be carried out if the instrument is operating under one of these conditions.

1) The illuminated area is characterized by large range distances (>1000 m) yielding to nonstationary APS conditions.
2) The temporal baseline between consecutive acquisitions is large enough to introduce significant atmospheric disturbances along the same daily data set. This temporal baseline may be on the order of several minutes or up to few seconds, depending on the characteristics and extension of the monitored area.
3) The APS does not remain stable due to boundary conditions. This occurs, i.e., when measures are carried out during dawn or sunset, even in small-scale areas of observation, or when the instrument is operating over mountainous environments, which are characterized by changing atmospheric conditions highly dynamic along the temporal axis.

Several studies presented in the last few years have been focused on estimating APS in GB-SAR measurements. They can divided in three main categories.

1) Some solutions are based on modeling the APS over the stable permanent scatterers (PSs) [22] or high-coherence points [41], [43] with no external sources of information.
2) Other solutions are based on obtaining APS dynamics from known motionless ground control points (GCP) [18], through the exploitation of available *a priori* knowledge of the area of interest.
3) Finally, some solutions are based on on-site meteorological information obtained over the monitored area [42].

From all these methods, model-based solutions proved to be very effective both in terms of complexity and its capacity to reach good results with no extra meteorological data or selection of stable GCPs over the area of interest. This is the solution implemented in the RiskSAR processing chain.

Model-based solutions explain the physical presence of APS through the modulation of the electromagnetic (EM) wave's velocity from the refractivity index N. With GB-SAR sensors, the medium to consider is the troposphere and N strictly depends on the atmospheric parameters of temperature, pressure, and humidity [44]. Under this approximation, $\varphi_{n,APS}(t)$ is obtained from the integration of the refractivity function N along the path L, which links the radar to the target [43]

$$\varphi_{n,APS}(t) = 10^{-6} \cdot \frac{4\pi f_c}{c} \int_L N(\vec{r_n}, t)dl. \quad (3)$$

At this point, two different scenarios shall be considered to fix the model.

1) In the presence of soft topography, for instance, in urban areas, a constant refractivity index N for the whole scene [41] is supposed. When this assumption of atmosphere spatial homogeneity is fulfilled, the projection of the high-coherence phase-differences onto the range direction exhibits a linear behavior. Hence, the atmospheric phase contribution, considering different atmospheric

conditions at times t_1 and t_2, is computed through the estimation of a simple phase-ramp, which is theoretically described by a slope coefficient [41] as it is illustrated in the following expression

$$\begin{aligned}\widehat{\Delta}\varphi_{n,APS}(t_1, t_2) &= \varphi_{n,APS}(t_2) - \varphi_{n,APS}(t_1)\\ &= 10^{-6} \cdot \frac{4\pi f_c r_n}{c} \cdot (N(t_2) - N(t_1))\\ &= 10^{-6} \cdot \frac{4\pi f_c r_n}{c} \cdot \Delta N.\end{aligned} \quad (4)$$

2) Recent studies demonstrate that linear-model-based solutions fail over mountainous regions in presence of steep topography [43], [45], [46]. In these areas, high-atmospheric disturbances, deeply correlated with the topography and highly dynamic in time, are present. For this reason, a generalization of the linear method seen above, and recently presented in [43], has been implemented in the RiskSAR processing chain. The spatial homogeneity assumption adopted in [41] is not fulfilled over this type of scenarios, where large variations in temperature, pressure, and humidity linked to height differences may be appreciated along the scene. Under these conditions, the distribution of the refractivity index N through the whole troposphere is modeled as a multilayer medium [44]

$$N(h) = N_S \cdot e^{-\alpha h} \quad (5)$$

where h refers to as the height above the ground, N_S is the surface value of the refractivity index, and α accounts for the inverse of a height scale factor in km^{-1}.

For small-scale scenarios, the refractivity index can be linearized with the first two terms of its Taylor series expansion [43]

$$N(h) = N_S - N_S \cdot \alpha \cdot h = N_S + N_1 \cdot h. \quad (6)$$

The absolute delay of the backscattered wave at each range distance will have now a term related with the range distance, as in the previous case, but also a second-order one depending on the product of range distance by height [43]

$$\widehat{\Delta}\varphi_{n,APS}(t_1, t_2) = \beta_1 \cdot r_n + \beta_2 \cdot h_n \cdot r_n \quad (7)$$

where β_1 and β_2 are defined as

$$\begin{aligned}\beta_1 &= \frac{4\pi f_c}{c} \cdot 10^{-6} \cdot \Delta N_R(t_1, t_2)\\ \beta_2 &= \frac{2\pi f_c}{c} \cdot 10^{-6} \cdot \Delta N_1(t_1, t_2)\end{aligned} \quad (8)$$

and N_R is the refractivity index at the radar height.

Using an external digital elevation model (DEM), and solving a multiple linear regression (MLR) equation system [43], the APS can be estimated.

Once a model solution is selected depending on the scenario images must be compensated for. Since images belonging to the same daily data set are characterized by having a short

temporal span and the displacement rate is supposed to be low, no displacements are expected to occur in a day. This means that the interferometric phase information is totally free of any deformation contribution. Under this assumption, the APS compensation technique may be carried out over all the high-coherence points of the scene. Typical values consist on selecting those points with coherences values over $0.9 - 0.95$ using a 9×9 multilook. The procedure to obtain the compensated phase $\varphi_{n,comp}$ is based on selecting a reference SLC image, referred to as master (at instant t_M), and then the rest of $M_i - 1$ SLC images, referred to as slaves (at instants t_S), are compensated with respect to the selected master with one of the model-based approaches presented before

$$\varphi_{n,comp}(t_S) = \arg\left(e^{j\varphi_n(t_S)} \cdot e^{-j\widehat{\Delta\varphi}_{n,APS}(t_M, t_S)}\right). \quad (9)$$

In the particular case of working with PolSAR data, a polarimetric calibration process is mandatory after the APS compensation process. This calibration is typically performed using a corner reflector, characterized by having a strong copolar response, and a cross-polar point-like target located at the near range [47], [48].

Once the APS phase term is removed from all the SLCs and data are properly calibrated, the SNR is improved performing a coherent sum of the whole daily data set. Since the coherent averaging is carried out along the temporal domain, the spatial resolution of the original images is preserved.

V. LONG-TERM PROCESSING

The objective of this second block, referred to as long-term processing (LTP), is to compensate the impact of the larger atmospheric artifacts among the N different daily time-averaged images obtained in the previous STP step. In addition and to cope with the more noticeable temporal decorrelation, it also tries to maximize the number of scatterers with good phase quality along time that reverts in a better APS compensation. Fig. 6 shows the block diagram of the LTP block.

Compared with the previous STP block, the APS compensation and estimation process become now more complex. Indeed, the temporal baseline between the N different time-averaged images is now larger and the interferograms may now be affected by displacements. In order to avoid a corrupted estimation of the APS, only the motion-less points of stable areas should be used. For this reason, an *a priori* knowledge of the area of interest is needed in order to help identifying stable areas. This information can be obtained in the field with conventional techniques and devices, such as leveling, inclinometers, extensometers, or piezometers.

Moreover, the larger temporal spans among images increase the chances of temporal decorrelation, especially in vegetated areas, and reduce the number of pixels useful for interferometric processing. This fact may compromise the estimation of the APS.

In this framework, a new strategy to improve the APS estimation and compensation process that makes use of the shortest temporal baselines available is proposed. Following the previous argument, a basis of $N - 1$ compensation
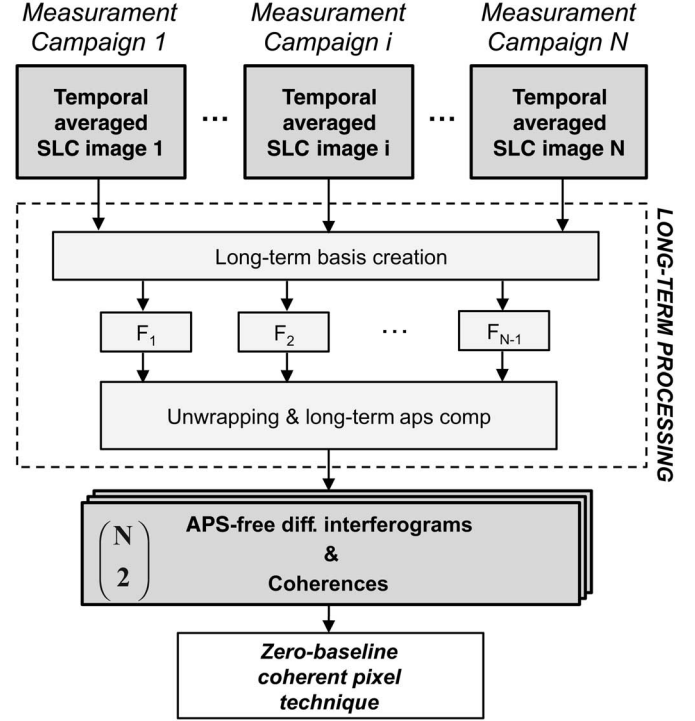

Fig. 6. Long-term processing (LTP) chain for the phase unwrapping, estimation of the long-term APS artifacts, and interferogram generation.

functions F between consecutive daily temporal-averaged images is employed. This strategy minimizes the loss of coherence [34], [43]

$$F(i, i+1) = e^{j\widehat{\Delta\varphi}^{APS}(i,i+1)} \quad (10)$$

where $\widehat{\Delta\varphi}_{APS}(i, i+1)$ refers to the model-based estimated APS for the consecutive measurements days i and $i + 1$.

Under this formulation, the compensating function $F(k, l)$ corresponding to the long-term interferogram computed from a pair of nonconsecutive daily temporal-averaged images k and l can be calculated by multiplying the basis compensation functions from the measurement days from k to l as follows [34], [43]:

$$F(k, l) = \prod_{j=k}^{l-1} F(i, i+1). \quad (11)$$

Consequently, the APS-free compensated interferometric phase $\Delta\varphi_{comp}(k, l)$ can be obtained using the compensating function calculated previously as follows:

$$\Delta\varphi_{comp}(k, l) = \arg\left(S_k \cdot S_l^* \cdot F^*(k, l)\right) \quad (12)$$

where S_k and S_l refer to the complex values from the same pixels in the first and in the second image that form the interferogram, respectively, and $*$ indicates the complex conjugate operator.

Furthermore, the use of PolSAR data has been recently proposed, as an additional and complementary strategy, to increase the quality and number of pixels during the APS estimation process [43]. The atmospheric behavior is independent of the

EM wave polarization at X-, C,- and Ku-bands. The rationale is to select for each interferogram the polarimetric channel providing the highest value of coherence [43]. The original three single-polarimetric interferograms are hence reduced to an optimized single one that provides the best response in terms of coherence.

It must be pointed out that prior the APS compensation step, all interferograms must be spatially unwrapped in order to carry out a correct fitting of the model. In this context, some unwrapping errors may appear if the terrain is complex or the illuminated area covers large-range distances. In order to face this problem, an outlier rejection process is proposed [43]. First, all the pixels fulfilling the high-coherence requirement ($\gamma > 0.9 - 0.95$) are used for a rough estimation of the model parameters. Once the model is estimated, these points are employed for the calculation of the standard deviation of the fitting error S. All the points accounting for a distance between the model and the interferometric phase greater than S are removed. The objective is twofold. On the one hand, this condition is imposed to prevent the inclusion of phase-instable scattererers during the estimation process. On the other hand, the phases affected by unwrapping errors, which are not expected to fit the APS model, are also removed. A better estimation of the APS is finally achieved by carrying out a second estimation using the remaining trustworthy pixels free of outliers and unwrapping errors.

Finally, it is worth mentioning that GB-SAR acquisitions over urban environments are typically characterized by high-reflectivity fluctuations induced by human activities [49]. If PolSAR data are available, the method proposed in [50] may be applied in order to improve even more the GB-InSAR processing. This method consists on an improved short-term filtering technique based on the detection of stable long-term Pauli-based polarimetric patterns [34]. In essence, a short-term filtering for the generation of the time-averaged SLC images is carried out by detecting the long-term polarimetric behaviors at pixel level providing the highest number of samples for each measurement day. In this work, a new concept of polarimetric entropy in time is also put forward to assess the benefits of the proposed technique with respect to the full short-term averaging process typically applied to distributed scattereres in natural environments [50]. On the one hand, this technique may be employed in order to obtain an improved time-averaged SLC image from each daily data set taking into account the polarimetric stability of point-like scatterers during the STP block. On the other hand, the higher quality of the time-averaged pixels is likely to lead to an improved long-term APS estimation.

VI. ZERO-BASELINE COHERENT PIXEL TECHNIQUE

Once the effects of the atmospheric artifacts have been compensated for, advanced PSI techniques may be adapted to work with the resulting zero-baseline APS-free interferograms generated in the previous steps. Among the multiple advanced PSI techniques developed by the remote sensing community during the last decade [4]–[15], the RiskSAR processing chain employs the CPT [4], [38].
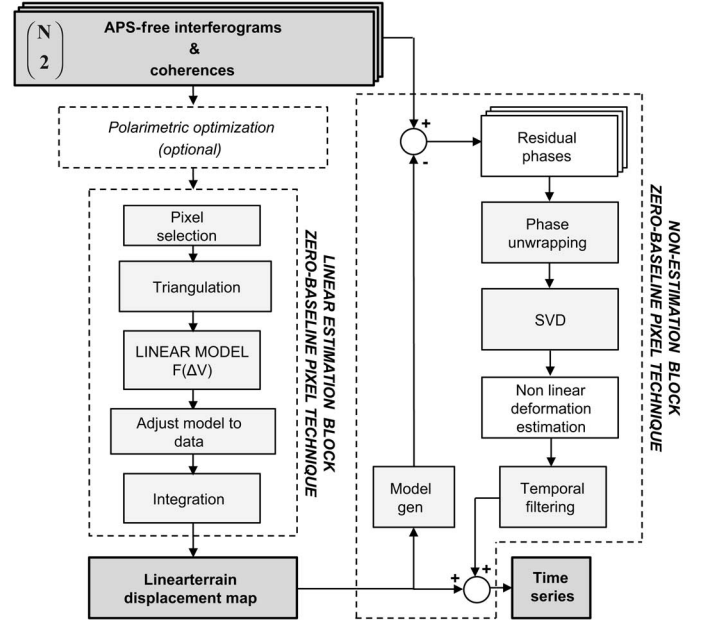

Fig. 7. Zero-baseline CPT processing chain.

This technique has been widely employed in the last years for the monitoring of several ground displacement episodes, using SAR data collected by spaceborne sensors, allowing the estimation of the linear and nonlinear components of displacement, the topographic error of the DEM used in the generation of the differential interferograms and the APS from a multitemporal set of differential interferograms [4], [38].

This section presents the adaptation of the CPT technique to work with zero-baseline fully-polarimetric GB-SAR data, highlighting the latest developments included. Fig. 7 shows the block diagram of the zero-baseline CPT.

A. Pixel Selection and Polarimetric Optimization

The reliability of any PSI technique is compromised by the phase quality of the interferograms involved in the processing. Mainly due to temporal decorrelation phenomena, only a limited number of pixels have enough phase quality for its reliable PSI processing. For this reason, prior to the application of any PSI technique, an adequate selection of high-quality pixel candidates is mandatory.

Two main criteria are available in the literature for the estimation of the pixels' phase quality: the coherence stability [4], [12] and the amplitude dispersion [6].

In the former approach, the interferometric phase quality of each pixel is estimated, through the calculation of the interferometric coherence [51]

$$\gamma = |\gamma|\, e^{j\varphi} = \frac{E\left\{S_1 \cdot S_2^*\right\}}{\sqrt{E\left\{|S_1|^2\right\} \cdot \left\{|S_2|^2\right\}}} \qquad (13)$$

where S_1 and S_2 are the complex values corresponding to the same pixel of the acquisitions forming an interferogram, $|\cdot|$ indicates the absolute value operator, and $E\left\{\cdot\right\}$ refers to as the expectation value. In practice, considering locally stationary

processes and under the assumption of ergodicity, the expectation operator is replaced by a spatial averaging around the pixel of interest, i.e., the multilook, to obtain the maximum likelihood estimator of the coherence $\hat{\gamma}$ [52].

There is a direct relationship between coherence values and the standard deviation of interferometric phases [51], [52]. Coherence values range between 0 and 1, attending these values to the limit situations of totally uncorrelated and correlated data, respectively. Typically, those targets characterized by having coherence values greater than a certain threshold of quality (typically $0.6-0.8$ depending on the multilook employed) in a large number of interferograms are selected as reliable for the later PSI processing [51].

Another approach to obtain temporal sensitivity along the whole stack of N_{int} interferograms consists on carrying out a temporal-average $\hat{\gamma}_t$ of the interferometric coherences $\hat{\gamma}$

$$|\hat{\gamma}_t| = \frac{2}{N(N-1)} \sum_{i=1}^{N_{\text{int}}} |\hat{\gamma}|. \tag{14}$$

Again, a minimum threshold of mean coherence is fixed and only those pixels presenting coherence values above this established threshold are selected for the later PSI processing. The coherence stability approach is more suited for selecting distributed scatterers, however, it also performs well for the selection of deterministic ones, especially when working at high frequencies such as X- or Ku-band.

The later approach is more suited for the selection of point-like scatterers. In this case, the phase stability of pixels is estimated through their (D_A) index in those pixels exhibiting higher values of SNR [6]

$$D_A = \frac{\sigma_A}{m_A} \tag{15}$$

where m_A and σ_A refer to as the mean and the standard deviation of the amplitude temporal evolution, respectively.

Under this approach, the phase standard deviation is proportional to the D_A index for high values of SNR. This technique looks for the so-called permanent scatterers (PS), which behave as deterministic point-like scatterers along the whole stack of SAR images and, theoretically, are not affected by decorrelation sources. Typically, those targets characterized by having a D_A lower than 0.25 are selected as reliable for the later PSI processing [6].

Finally, a new estimator to evaluate the pixels' phase quality, referred to as temporal sublook coherence (TSC), has been recently presented in [53] showing promising results for PSI applications. The nature of this estimator, which is based on exploiting the spectral properties of point-like scatterers through the coherence evaluation of different sublooks of the image spectrum, also allows the detection of the deterministic point-like scatters available in the area of interest. In contrast to the PS approach, this method is not affected by amplitude fluctuations and hence does not require any radiometric calibration. In addition, it provides a good tradeoff between preserving the spatial resolution of interferograms and performing reliable estimations of phase statistics when the number of SAR images is low.

During the last years, the CPT has been accordingly adapted to work with all these approaches. The choice of the pixel selection method depends on the intrinsic characteristics of the targets within the area of study and on the number of SAR acquisitions available. On the one hand, the coherence stability pixel selection criterion performs better under natural scenarios with predominance of distributed scatterers. This approach ensures reliable terrain displacement estimations, even when few numbers of interferograms are available. On the other hand, the D_A or the TSC pixel selection criteria performs better under urban areas with predominance of deterministic point-like scatterers, which are not affected by speckle noise. These two methods preserve the full-resolution of the images and are is usually applied over scenarios with predominance of man-made structures. Contrarily, the coherence stability pixel selection method requires performing a multilook of the interferograms, as seen previously, with its consequent loose of spatial resolution. The main limitation of the D_A approach is that it requires larger numbers of images to be reliable, typically more than 20 [6].

To face temporal decorrelation phenomena and enhance the phase quality of interferograms, the CPT has been recently adapted to work with PolSAR data. Prior the pixel selection step, the processing may be benefited by the exploitation of polarimetric information. In the classical PSI formulation, only a single-polarimetric channel is considered. This means that all pixels involved in the processing belong to the same polarimetric channel. The objective of polarimetric optimization techniques is to enhance the phase quality of interferograms to significantly increase the number of pixel candidates.

Some works on polarimetric optimization have been recently developed by the SAR community for PSI purposes. The idea was originally introduced by the RSLab [54], [55] for its use in the data provided by the polarimetric RiskSAR sensor. For the first time, the use of polarimetric SAR Interferoemtry (PolInSAR) techniques for PSI purposes, which have demonstrated to outperform classical single-polarimetric performance, was proposed. The use of PolInSAR algorithms have been also extended and successfully applied to spaceborne data [56]–[58] in the last few years. A complete study of the different polarimetric optimization techniques and its application to PSI has been recently presented in [59]–[61].

Nowadays the RiskSAR processing chain works with the best, sub-optimum scattering mechanism (SOM) [62] and equal scattering mechanism (ESM) [63] polarimetric optimization methods [60]. All these methods are addressed to find a combination of the original polarimetric channels with the objective to optimize the coherence estimator, when multilooked data are employed, and the D_A or TSC, when working at full resolution.

In the best approach, for each pixel of the image, the polarimetric channel providing the best response in terms of phase quality is selected. Despite the significant improvement in terms of pixels' density achieved with this method, this strategy does not completely exploit the potentials of polarimetry. The objective of the other two approaches is to find the optimum scattering coefficient (ESM) or the best polarimetric basis transformation (SOM), applied along the whole PolSAR data set that maximizes the phase quality [60].

Regardless of the polarimetric optimization method and owing to the lack of topographic component in the GB-SAR interferometric phase, a single-baseline optimization process may be performed for each interferogram independently. In this case, the optimization is hence carried out at interferogram level with no risk of adding undesired phase terms due to changes in the phase centers within the same pixel. In the case of working with multibaseline SAR data, a topographic component in the differential phase of the interferograms appears. In this case, the optimization must be carried out ensuring the same polarimetric mechanism for all the data set. Optimizing them independently as in the GB-SAR case would lead to changes in the phase centers within the same pixel, corrupting the final displacement maps retrieved.

Summarizing, each pair of acquisitions produces three interferograms, one per polarimetric channel. After applying any of the polarimetric optimization techniques seen above, the three interferograms are reduced to a single one with an optimum response in terms of phase quality. This process gives place to a significant increase in terms of pixel candidates for the later processing. Once the interferograms are optimized, classical PSI algorithms can be applied to the new stack of optimized interferograms, with no practical differences with respect to the single-polarimetric case. The best performance in terms of pixels' density and phase quality is reached with the ESM approach but it requires the higher computational cost [60].

B. Triangulation, Minimization, and Integration

Once the pixel candidates have been selected, the next step consists on carrying out a Delaunay triangulation [64]. The objective of the triangulation is to work with phase increments among pixels instead of absolute phases. This step is also important to avoid phase unwrapping at this stage. Assuming a high density of pixel candidates (above 10^4 pixels/km^2), the phase increments may reasonably be supposed to have a value lower than π radians in most of the interferograms. As it will be detailed later, the model adjustment is not affected by having wrapped phases in some of the interferograms. When some areas do not have the required density or different clusters of pixels appear, redundant network strategies may be employed. In this case, pixel candidates are connected uniformly in all directions up to a maximum number of arcs forming a spider web-like network, which adds redundancy to the system. Finally, since APS change smoothly in space, the possible remaining atmospheric artifacts present in the zero-baseline interferograms are also minimized thanks to the triangulation.

When nonzero-baseline interferograms are available, the interferometric phase increment $\Delta\varphi_{m,n}$ between two connected points P_m and P_n by the triangulation can be expressed for the ith interferogram as the contribution of the following terms [4], [38]:

$$\Delta\varphi_{m,n}(T_i, B_{n,i}) = \frac{4\pi}{\lambda} \cdot T_i \cdot (v(x_m, y_m) - v(x_n, y_n))$$
$$+ \frac{4\pi}{\lambda} \cdot \frac{B_{n,i}}{R_i \sin\theta_i} \cdot (\varepsilon(x_m, y_m) - \varepsilon(x_n, y_n))$$
$$+ \Delta\varphi_{m,n}^{res} \quad (16)$$

where (x_m, y_m) and (x_n, y_n) indicate the coordinates of the nodes forming the $arc_{m,n}$, $v(x_m, y_m) - v(x_n, y_n)$, and $\varepsilon(x_m, y_m) - \varepsilon(x_n, y_n)$ refer to the increment of linear displacement rate and topographic error, λ indicates the wavelength, T_i and B_i are the temporal and spatial baselines, respectively, R_i is the sensor to target distance, θ_i the incidence angle, and $\Delta\varphi_{m,n}^{res}$ account for the atmospheric, nonlinear, and noise components of the phase.

As GB-SAR sensors work under a zero-baseline configuration, the phase term due to the topographic error component is not necessary. Likewise, there are no APS contributions in the residue since they were compensated previously. The interferometric phase increment expression seen in (16) may hence be simplified in the following way

$$\Delta\varphi_{m,n}(T_i) = \frac{4\pi}{\lambda} \cdot T_i \cdot (v(x_m, y_m) - v(x_n, y_n)) + \Delta\varphi_{m,n}^{res} \quad (17)$$

where now $\Delta\varphi_{m,n}^{res}$ accounts only for the nonlinear and noise components of the phase.

At this point, a linear model $\Delta\varphi_{m,n}^{\text{mod } el}$ is defined for each arc of the triangulation in order to estimate the linear displacement rate of the deformation process

$$\Delta\varphi_{m,n}^{\text{model}}(T_i) = \frac{4\pi}{\lambda} \cdot T_i \cdot \Delta v \quad (18)$$

where $\Delta v = v(x_m, y_m) - v(x_n, y_n)$ refers to the increment of linear displacement rate.

In order to find Δv for each arc, the defined model is adjusted to the data observations through the minimization of a cost function defined in the complex plane and addressed as model adjustment function (MAF) Γ [4], [38]

$$\Gamma_{m,n}(v) = \frac{2}{N \cdot (N-1)}$$
$$\left| \sum_{i=1}^{N \cdot (N-1)/2} e^{j\Delta\varphi_{m,n}(T_i)} - e^{j\Delta\varphi_{m,n}^{\text{mod } el}(T_i)} \right|^2. \quad (19)$$

The minimization is carried out using the conjugate gradient method (CGM) [65], and once it is performed for each arc, the result is a set of velocities' increments for each selected pixel. As the model adjustment is done in the complex plane, with a uniform distribution of temporal baselines, it is not a problem that some of the interferograms of an arc have wrapped phases.

At this stage, the MAF is used to estimate the quality of solutions. Γ lies inside the $[0, 1]$ interval. It reaches the maximum value when the linear model perfectly fits the data, and tends to zero in presence of a poor model adjustment. The MAF values for each arc are used to discard pixels with poor adjustment to the linear model. This is mainly produced in those pixels affected by displacements characterized by strong non-linearities. After this process, those pixels which are left isolated are removed as well. Another iteration of the minimization process is carried out with the surviving arcs. At this point, the absolute values of velocity v for each pixel are calculated through an integration process. As the solution is floating, one

or multiple seeds with known velocities are used as tie points during the integration [4], [38].

It is worth pointing out that the accuracy of the estimated linear displacement strongly depends on the density and quality of the selected pixels. To face this problem, the CPT algorithm includes a multilayer processing [38] to preserve the accuracy of the pixels with the highest quality and benefit those with the lowest quality. The method is based on dividing the selected pixels in different layers according to their phase quality. Beginning with the top layer, the linear block is iteratively processed by adding the successive low-quality layers. Once the absolute velocity values are obtained from a layer, they are fixed and used as seeds in the following successive integration processes. With this approach, the density of pixels is largely improved but the quality of the PSI results for the best pixels is not affected by the low quality ones [38].

C. Time Series

The objective of the last step of the CPT algorithm is to obtain the nonlinear component of the displacement, also known as timeseries.

For this purpose, the phase component $\Delta\varphi_{\mathrm{model}}$ corresponding to the linear model calculated above is subtracted from the original interferometric phases $\Delta\varphi$, leading to the so-called phase residues $\Delta\varphi_{residue}$

$$\Delta\varphi_{residue}(T_i) = \Delta\varphi(T_i) - \Delta\varphi_{\mathrm{model}}(T_i). \qquad (20)$$

In orbital-based PSI, the residues account for both the nonlinear component and the atmospheric artifacts. In order to isolate both components a common strategy is based on carrying out a filtering process, taking advantage of their particular temporal and spatial frequency behaviors [51]. A large number of images is required to achieve reliable nonlinear estimation processes. Contrarily, the residues in the GB-SAR case are only composed by the nonlinear displacement term. Since no filtering process is required, a reliable estimation of the nonlinear component may be achieved, even when a reduced number of images is available.

The following step to obtain the nonlinear contribution of the displacement is based on carrying out a temporal phase unwrapping of the resulting residues. Since these are expected to behave smoothly in both the spatial and the temporal domains, the phase unwrapping is less complex at this stage. The reason is that the linear contribution has been removed and atmospheric artifacts are expected not to be present in the phase residues.

Once the unwrapping is carried out, it only remains to obtain the interferometric phases the phase of each single image of the data set

$$\Delta\varphi_{residue}(T_i) = \varphi_{residue}(TM_i) - \varphi_{residue}(TS_i) \qquad (21)$$

where TM_i and TS_i refer to as the master and slave times belonging to the ith interferogram, respectively. These unwrapped residues must be reordered in time and added to the model for obtaining the complete description of the nonlinear temporal evolution of the deformation. In this context,

the single value descomposition (SVD) algorithm is applied to solve this linear system of equations [4], [38].

Finally, the sum of the linear and nonlinear contribution leads to the total displacement evolution or time series of the deformation process. Optionally, time series can be temporally filtered in order to reduce the remaining noise.

At this stage, both the linear estimation and the final time series can be geocoded in Universal Traversal Mercator (UTM) coordinates and be visualized by using geographical information system (GIS) software or a virtual globe viewer.

VII. Conclusion

This paper has focused on both the GB-SAR hardware architecture and the GB-InSAR processing developed at the RSLab during the last years. The objective has been to summarize the key characteristics of these sensors and the processing chain for ground displacement monitoring applications. First, a brief description of the RiskSAR hardware, highlighting the advantages of working with stepped linear frequency modulated continuous wave signals, has been given. Later, the whole GB-InSAR processing chain for PSI has been widely discussed.

All the developments described have been focused on the GB-SAR sensor working in a discontinuous operation mode. This may be seen as a generalization of the continuous operation mode but requires a more complex processing chain.

The way to obtain a single time-averaged SLC image from each measurement day has initially been described. The main benefit of this approach is the improvement of the SNR of time-stationary targets. Then, the different alternatives to compensate the APS in GB-SAR measurements along both short-term and long-term temporal spans have been discussed. Performing a correct APS estimation and compensation step has been demonstrated to be a key step for correct displacement estimations. The adaptation of the CPT to work with either single- or fully polarimetric zero-baseline data has been also presented. The redundancy provided by the polarimetric data allows to increase the number of pixels with enough phase quality for the interferometric processing. Higher pixel densities also allow better APS estimation and compensation and a better estimation of both the linear and nonlinear terms of deformation.

In part II of this paper [39], the hardware and the processing chain are applied to two different scenarios: an urban area with mining induced subsidence and a landslide that is being reactivated with periods of strong rainfalls. The processing of the acquired data will shown the capabilities of GB-SAR sensors for monitoring different kinds of displacement phenomena. The obtained results will be deeply analyzed, discussed, and validated with ground-truth data.

References

[1] D. Massonnet and K. L. Feigl, "Radar interferometry and its application to changes in the Earth's surface," *Rev. Geophys.*, vol. 36, no. 4, p. 441, 1998.

[2] R. Bürgmann, P. A. Rosen, and E. J. Fielding, "Synthetic aperture radar interferometry to measure Earth's surface topography and its deformation," *Annu. Rev. Earth Planet. Sci.*, vol. 28, no. 1, pp. 169–209, May 2000.

This article has been accepted for inclusion in a future issue of this journal. Content is final as presented, with the exception of pagination.

12   IEEE JOURNAL OF SELECTED TOPICS IN APPLIED EARTH OBSERVATIONS AND REMOTE SENSING

[3] A. K. Gabriel, R. M. Goldstein, and H. A. Zebker, "Mapping small elevation changes over large areas: Differential radar interferometry," *J. Geophys. Res.*, vol. 94, no. B7, p. 9183, 1989.

[4] O. Mora, J. Mallorqui, and A. Broquetas, "Linear and nonlinear terrain deformation maps from a reduced set of interferometric SAR images," *IEEE Trans. Geosci. Remote Sens.*, vol. 41, no. 10, pp. 2243–2253, Oct. 2003.

[5] A. Ferretti, C. Prati, and F. Rocca, "Nonlinear subsidence rate estimation using permanent scatterers in differential SAR interferometry," *IEEE Trans. Geosci. Remote Sens.*, vol. 38, no. 5, pp. 2202–2212, Sep. 2000.

[6] A. Ferretti, C. Prati, and F. Rocca, "Permanent scatterers in SAR interferometry," *IEEE Trans. Geosci. Remote Sens.*, vol. 39, no. 1, pp. 8–20, Jan 2001.

[7] O. Mora, J. J. Mallorqui, and J. Duro, "Generation of deformation maps at low resolution using differential interferometric SAR data," in *Proc. IEEE Int. Geosci. Remote Sens. Symp.*, 2002, vol. 5, pp. 2696–2698.

[8] P. Berardino, G. Fornaro, R. Lanari, and E. Sansosti, "A new algorithm for surface deformation monitoring based on small baseline differential SAR interferograms," *IEEE Trans. Geosci. Remote Sens.*, vol. 40, no. 11, pp. 2375–2383, Nov. 2002.

[9] C. Werner, U. Wegmuller, T. Strozzi, and A. Wiesmann, "Interferometric point target analysis for deformation mapping," in *Proc. IEEE Int. Geosci. Remote Sens. Symp. (IGARSS'03)*, 2003, vol. 7, pp. 4362–4364.

[10] A. Arnaud *et al.*, "ASAR ERS interferometric phase continuity," in *Proc. IEEE Int. Geosci. Remote Sens. Symp. (IGARSS'03)*, 2003, vol. 2, pp. 1133–1135.

[11] A. Hooper, "A new method for measuring deformation on volcanoes and other natural terrains using InSAR persistent scatterers," *Geophys. Res. Lett.*, vol. 31, no. 23, p. L23611, 2004.

[12] R. Lanari *et al.*, "A small-baseline approach for investigating deformations on full-resolution differential SAR interferograms," *IEEE Trans. Geosci. Remote Sens.*, vol. 42, no. 7, pp. 1377–1386, Jul. 2004.

[13] A. Hooper, "A multi-temporal InSAR method incorporating both persistent scatterer and small baseline approaches," *Geophys. Res. Lett.*, vol. 35, no. 16, p. L16302, Aug. 2008.

[14] G. Fornaro, D. Reale, and F. Serafino, "Four-dimensional SAR imaging for height estimation and monitoring of single and double scatterers," *IEEE Trans. Geosci. Remote Sens.*, vol. 47, no. 1, pp. 224–237, Jan. 2009.

[15] A. Ferretti *et al.*, "A new algorithm for processing interferometric data-stacks: SqueeSAR," *IEEE Trans. Geosci. Remote Sens.*, vol. 49, no. 9, pp. 3460–3470, Sep. 2011.

[16] D. Tarchi *et al.*, "SAR interferometry for structural changes detection: A demonstration test on a dam," in *Proc. IEEE Int. Geosci. Remote Sens. Symp. (IGARSS'99)*, 1999, vol. 3, pp. 1522–1524.

[17] H. Rudolf, D. Leva, D. Tarchi, and A. Sieber, "A mobile and versatile SAR system," in *Proc. IEEE Int. Geosci. Remote Sens. Symp. (IGARSS'99)*, 1999, vol. 1, pp. 592–594.

[18] D. Leva, G. Nico, D. Tarchi, J. Fortuny-Guasch, and A. Sieber, "Temporal analysis of a landslide by means of a ground-based SAR interferometer," *IEEE Trans. Geosci. Remote Sens.*, vol. 41, no. 4, pp. 745–752, Apr. 2003.

[19] G. Nico, D. Leva, G. Antonello, and D. Tarchi, "Ground-based SAR interferometry for terrain mapping: Theory and sensitivity analysis," *IEEE Trans. Geosci. Remote Sens.*, vol. 42, no. 6, pp. 1344–1350, Jun. 2004.

[20] S. Brown, S. Quegan, K. Morrison, J. Bennett, and G. Cookmartin, "High-resolution measurements of scattering in wheat canopies-implications for crop parameter retrieval," *IEEE Trans. Geosci. Remote Sens.*, vol. 41, no. 7, pp. 1602–1610, Jul. 2003.

[21] G. Luzi *et al.*, "Ground-based radar interferometry for landslides monitoring: Atmospheric and instrumental decorrelation sources on experimental data," *IEEE Trans. Geosci. Remote Sens.*, vol. 42, no. 11, pp. 2454–2466, Nov. 2004.

[22] L. Noferini *et al.*, "Permanent scatterers analysis for atmospheric correction in ground-based SAR interferometry," *IEEE Trans. Geosci. Remote Sens.*, vol. 43, no. 7, pp. 1459–1471, Jul. 2005.

[23] M. Pieraccini, G. Luzi, and C. Atzeni, "Ground-based interferometric SAR for terrain elevation mapping," *Electron. Lett.*, vol. 36, no. 16, pp. 1416–1417, 2000.

[24] Z.-S. Zhou, W.-M. Boerner, and M. Sato, "Development of a ground-based polarimetric broadband SAR system for noninvasive ground-truth validation in vegetation monitoring," *IEEE Trans. Geosci. Remote Sens.*, vol. 42, no. 9, pp. 1803–1810, Sep. 2004.

[25] C. Del Ventisette *et al.*, "Using ground based radar interferometry during emergency: The case of the A3 motorway (Calabria Region, Italy) threatened by a landslide," *Natural Hazards Earth Syst. Sci.*, vol. 11, no. 9, pp. 2483–2495, Sep. 2011.

[26] H. Lee, S. Member, J.-H. Lee, S. Member, and K.-E. Kim, "Development of a truck-mounted arc-scanning synthetic aperture radar," *IEEE Trans. Geosci. Remote Sens.*, vol. 52, no. 5, pp. 2773–2779, May 2014.

[27] G. Bernardini, P. Ricci, and F. Coppi, "A ground based microwave interferometer with imaging capabilities for remote measurements of displacements," in *Proc. 7th Geomatic week*, Barcelona, Spain, 2007.

[28] P. Farina *et al.*, "IBIS-M: An innovative radar for monitoring slopes in open-pit mines," in *Proc. Int. Symp. Rock Slope Stabil. Open Pit Mining Civil Eng.*, Vancouver, BC, Canada, 2011 [Online]. Available: https://www.idscorporation.com/images/Downloads/GeoRadar/IBIS_White_Papers/slopePaper190.pdf

[29] O. Montserrat, "Deformation measurement and monitoring with ground-based SAR," Ph.D. dissertation, Institute of Geomatics, Barcelona, Spain, 2012.

[30] P. Farina and N. Coli, "Efficient real time stability monitoring of mine walls: The Çöllolar Mine case study," in *Int. Mining Congr. Exhib. Turkey*, Antalya, Turkey, 2013, pp. 111–117.

[31] M. Crosetto, O. Monserrat, G. Luzi, M. Cuevas-González, and N. Devanthéry, "Discontinuous GBSAR deformation monitoring," *ISPRS J. Photogramm. Remote Sens.*, vol. 93, pp. 136–141, Jul. 2014.

[32] A. Aguasca, A. Broquetas, J. J. Mallorqui, and X. Fabregas, "A solid state L to X-band flexible ground-based SAR system for continuous monitoring applications," in *Proc. IEEE Int. Geosci. Remote Sens. Symp., 2004 (IGARSS'04)*, 2004, vol. 2, pp. 757–760.

[33] L. Pipia, A. Aguasca, X. Fabregas, and J. Mallorqui, "A polarimetric ground-based SAR system: First results at X-band," in *URSI Comm. F Symp. Microw. Remote Sens. Earth, Oceans, Ice, Atmos.*, Ispra, Italy, Jul. 2005.

[34] L. Pipia, "Polarimetric differential SAR interferometry with ground-based sensors," Ph.D. dissertation, Universitat Politècnica de Catalunya, Barcelona, Spain, 2009.

[35] C. Werner, T. Strozzi, A. Wiesmann, and U. Wegmüller, "GAMMA's portable radar interferometer," in *Proc. 13th FIG Symp. Deform. Meas. Anal.*, 2008, pp. 1–10.

[36] S. Rodelsperger, A. Coccia, D. Vicente, and A. Meta, "Introduction to the new metasensing ground-based SAR: Technical description and data analysis," in *Proc. IEEE Int. Geosci. Remote Sens. Symp.*, Jul. 2012, pp. 4790–4792.

[37] K. Lukin and A. Mogyla, "Monitoring of St. Sophia Cathedral interior using Ka-band ground based noise waveform SAR," in *Proc. 6th Radar Conf. (EURAD'09)*, Rome, Italy, 2009, pp. 215–217.

[38] P. Blanco-Sánchez, J. J. Mallorquí, S. Duque, and D. Monells, "The Coherent Pixels Technique (CPT): An advanced DInSAR technique for nonlinear deformation monitoring," *Pure Appl. Geophys.*, vol. 165, no. 6, pp. 1167–1193, Aug. 2008.

[39] R. Iglesias *et al.*, "Ground-based polarimetric SAR interferometry for the monitoring of terrain displacement phenomena. Part II: Applications," to be published.

[40] M. Soumekh, Synthetic Aperture Radar Signal Processing: With MATLAB Algorithms. Hoboken, NJ, USA: Wiley, 1999.

[41] L. Pipia, X. Fabregas, A. Aguasca, and C. Lopez-Martinez, "Atmospheric artifact compensation in ground-based DInSAR applications," *IEEE Geosci. Remote Sens. Lett.*, vol. 5, no. 1, pp. 88–92, Jan. 2008.

[42] L. Iannini and A. Monti Guarnieri, "Atmospheric phase screen in ground-based radar: Statistics and compensation," *IEEE Geosci. Remote Sens. Lett.*, vol. 8, no. 3, pp. 537–541, May 2011.

[43] R. Iglesias *et al.*, "Atmospheric phase screen compensation in ground-based SAR with a multiple-regression model over mountainous regions," *IEEE Trans. Geosci. Remote Sens.*, vol. 52, no. 5, pp. 2436–2449, May 2014.

[44] M. P. M. Hall, *Effects of the Troposphere on Radio Communication*. London, U.K.: The Institution of Electrical Engineers, 1979.

[45] X. Fabregas, R. Iglesias, A. Aguasca, and J. A. Gili, "2D atmospheric artifact compensation with multiple regression model in ground-based SAR over mountainous areas," in *Proc. 7th Int. Workshop Adv. Sci. Appl. SAR Interferometry (Fringe)*, Frascati, Italy, Sep. 2011.

[46] X. Fabregas, R. Iglesias, and A. Aguasca, "A new approach for atmospheric phase screen compensation in ground-based SAR over areas with steep topography," in *Proc. 9th Eur. Conf. Synth. Aperture Radar (EUSAR)*, Nuremberg, Germany, Apr. 2012, pp. 12–15.

[47] K. Sarabandi, F. Ulaby, and M. Tassoudji, "Calibration of polarimetric radar systems with good polarization isolation," *IEEE Trans. Geosci. Remote Sens.*, vol. 28, no. 1, pp. 70–75, Jan. 1990.

[48] F. T. Ulaby and C. Elachi, *Radar Polarimetry for Geoscience Applications*, A. H. Norwood, Ed. Norwood, MA, USA: Artech House, 1990.

[49] L. Pipia *et al.*, "Polarimetric temporal information for urban deformation map retrieval," in *Proc. 2007 IEEE Int. Geosci. Remote Sens. Symp. (IGARSS'07)*, Jul. 2007, pp. 192–195.

[50] L. Pipia, X. Fabregas, A. Aguasca, and C. Lopez-Martinez, "Polarimetric temporal analysis of urban environments with a ground-based SAR," *IEEE Trans. Geosci. Remote Sens.*, vol. 51, no. 4, pp. 2343–2360, Apr. 2013.

[51] R. Hanssen, Radar Interferometry: Data Interpretation and Error Analysis, Norwell, MA, USA: Kluwer, 2001.

[52] M. Seymour and I. Cumming, "Maximum likelihood estimation for SAR interferometry," in *Proc. IEEE Int. Geosci. Remote Sens. Symp. (IGARSS'94)*, 1994, vol. 4, pp. 2272–2275.

[53] R. Iglesias, J. Mallorqui, and P. Lopez-Dekker, "DInSAR pixel selection based on sublook spectral correlation along time," *IEEE Trans. Geosci. Remote Sens.*, vol. 52, no. 7, pp. 3788–3799, Jul. 2014.

[54] L. Pipia *et al.*, "Polarimetric differential SAR interferometry: First results with ground-based measurements," *IEEE Geosci. Remote Sens. Lett.*, vol. 6, no. 1, pp. 167–171, Jan. 2009.

[55] L. Pipia, X. Fabregas, A. Aguasca, C. Lopez-Martinez, and J. J. Mallorqui, "Polarimetric coherence optimization for interferometric differential applications," in *Proc. IEEE Int. Geosci. Remote Sens. Symp.*, 2009, pp. V-146–V-149.

[56] V. D. Navarro-Sanchez, J. M. Lopez-Sanchez, and F. Vicente-Guijalba, "A contribution of polarimetry to satellite differential SAR interferometry: Increasing the number of pixel candidates," *IEEE Geosci. Remote Sens. Lett.*, vol. 7, no. 2, pp. 276–280, Apr. 2010.

[57] V. D. Navarro-Sanchez and J. M. Lopez-Sanchez, "Subsidence monitoring using polarimetric persistent scatterers interferometry," in *Proc. IEEE Int. Geosci. Remote Sens. Symp.*, Jul. 2011, pp. 1083–1086.

[58] V. D. Navarro-Sanchez and J. M. Lopez-Sanchez, "Improvement of persistent-scatterer interferometry performance by means of a polarimetric optimization," *IEEE Geosci. Remote Sens. Lett.*, vol. 9, no. 4, pp. 609–613, Jul. 2012.

[59] V. D. Navarro-Sanchez, J. M. Lopez-Sanchez, and L. Ferro-Famil, "Polarimetric approaches for persistent scatterers interferometry," *IEEE Trans. Geosci. Remote Sens.*, vol. 52, no. 3, pp. 1667–1676, Mar. 2014.

[60] R. Iglesias *et al.*, "Phase quality optimization in polarimetric differential SAR interferometry," *IEEE Trans. Geosci. Remote Sens.*, vol. 52, no. 5, pp. 2875–2888, May 2014.

[61] R. Iglesias *et al.*, "Polarimetric optimization of temporal sublook coherence for dinsar applications," *IEEE Geosci. Remote Sens. Lett.*, vol. 12, no. 1, pp. 87–91, Jan. 2015.

[62] L. Sagués *et al.*, "Indoor experiments on polarimetric SAR interferometry," *IEEE Trans. Geosci. Remote Sens.*, vol. 38, no. 2, pp. 671–684, Mar. 2000.

[63] E. Colin, C. Titin-Schnaider, and W. Tabbara, "An interferometric coherence optimization method in radar polarimetry for high-resolution imagery," *IEEE Trans. Geosci. Remote Sens.*, vol. 44, no. 1, pp. 167–175, Jan. 2006.

[64] B. N. Delaunay, "Sur la sphère vide," *Bull. Acad. Sci. USSR*, vol. 7, no. 6, pp. 793–800, 1934.

[65] M. R. Hestenes and E. Stiefel, "Methods of conjugate gradients for solving linear systems," *J. Res. Nat. Bureau Standard*, vol. 49, no. 6, pp. 409–436, Dec. 1952.

Rubén Iglesias (S'12) was born in Barcelona, Spain, in 1982. He received the B.Sc. degree in telecommunication engineering from the Universitat Politècnica de Catalunya (UPC), Barcelona, Spain, in 2008, and is currently pursuing the Ph.D. degree, focusing on the development of advanced DInSAR and polarimetric DInSAR (PolDInSAR) techniques for the detection, monitoring, and characterization of slow-moving landslides with both orbital and ground-based SAR (GB-SAR) data from UPC.

From June 2009 to June 2010, he was with the Active Remote Sensing Unit, Institute of Geomatics, Barcelona, Spain, working in several projects related with the application of DInSAR to terrain-deformation monitoring with orbital and GB-SAR data. From June 2010 to March 2014, he was in the Signal Theory and Communications Department (TSC), UPC, working as a Research Assistant in the framework of DInSAR and GB-SAR DInSAR applications. In April 2014, he joined Altamira Information, an experienced Earth Observation company in Barcelona dedicated to provide ground displacement measurements solutions using DInSAR techniques.

Albert Aguasca (S'90–M'94) was born in Barcelona, Spain, in 1964. He received the M.Sc. and Ph.D. degrees in telecommunication engineering from the Universitat Politècnica de Catalunya (UPC), Barcelona, Spain, in 1989 and 1993, respectively.

Since 1995, he has been an Associate Professor with the School of Telecommunications Engineering, UPC. His teaching activities involve RF and microwave circuits for communications and radio navigation systems. He has published more than 40 papers on microwave SAR, radiometer systems, and microwave circuits. His research interests include the design and development of SAR and microwave radiometer systems for unmanned aerial vehicle (UAV) platforms, and also collaborates in the design and development of smart antennas and scavenging circuitry.

Xavier Fabregas (S'89–M'93) received the B.S. degree in physics from Barcelona University, Barcelona, Spain, in 1988, and the Ph.D. degree in applied sciences from the Universitat Politècnica de Catalunya (UPC), Barcelona, Spain, in 1995.

In 1990, he joined the Photonic and Electromagnetic Engineering Group, Signal Theory, and Communications Department, UPC. Since 1996, he has been an Associate Professor with UPC. In 2001, he spent an 8-month sabbatical with the Microwaves and Radar Institute (HR) of the German Aerospace Agency (DLR), Oberpfaffenhofen, Germany. He has published 26 international journal papers and more than 106 conference proceedings and has received a patent. He is a reviewer in several international journals. His research interests include polarimetric-retrieval algorithms, polarimetric calibration and speckle models, GB-SAR sensors and their applications, and time series for multidimensional SAR data applications for urban and terrain deformation monitoring.

Jordi J. Mallorqui (S'93–M'96–SM'13) was born in Tarragona, Spain, in 1966. He received the Ingeniero degree in telecommunications engineering and the Doctor Ingeniero degree in telecommunications engineering from the Department of Signal Theory and Communications, Universitat Politècnica de Catalunya (UPC), Barcelona, Spain, in 1990 and 1995, respectively.

Since 1993, he has been with the School of Telecommunications Engineering of Barcelona, UPC, first as an Assistant Professor, later in 1997 as an Associate Professor, and since 2011, as a Full Professor. His teaching activity involves microwaves, radionavigation systems, and remote sensing. He spent a sabbatical year with the Jet Propulsion Laboratory, Pasadena, CA, USA, in 1999, working on interferometric airborne SAR calibration algorithms. He is currently working on the application of SAR interferometry to terrain-deformation monitoring with orbital, airborne, and ground data; vessel detection and classification from SAR images; and 3-D EM simulation of SAR systems. He is also collaborating in the design and construction of a GB-SAR interferometer for landslide control. He has published more than 100 papers on microwave tomography, EM numerical simulation, and SAR processing, interferometry, and differential interferometry in refereed journals and international symposia.

Dani Monells (S'11) was born in Sant Joan de les Abadesses, Spain, in 1981. He received the M.Sc. degree in telecommunication engineering from the Universitat Politècnica de Catalunya (UPC), Barcelona, Spain, in 2008. He is currently pursuing the Ph.D. degree, focused on differential SAR interferometry (DInSAR) in orbital platforms, focusing on the exploitation of polarimetric SAR acquisitions (PolSAR), at the Signal Theory and Communications Department (TSC), UPC.

Since 2007, he has been working in several projects for the monitoring of terrain displacements and developing the TSC interferometric chain and processor, in order to give support to the new generation SAR satellites.

Carlos López-Martínez (S'97–M'04–SM'11) received the M.Sc. degree in electrical engineering and the Ph.D. degree in modelling and filtering of speckle noise in multidimensional SAR data from the Universitat Politècnica de Catalunya, Barcelona, Spain, in 1999 and 2003, respectively.

From October 2000 to March 2002, he was with the Frequency and Radar Systems Department (HR), German Aerospace Center (DLR), Oberpfaffenhofen, Germany. From June 2003 to December 2005, he has been with the Image and Remote Sensing Group— SAR Polarimetry Holography Interferometry Radargrammetry (SAPHIR) Team, Institute of Electronics and Telecommunications of Rennes (IETR), Rennes, France. In January 2006, he joined the Universitat Politècnica de Catalunya as a Ramn-y-Cajal researcher, Barcelona, Spain, where he is currently an Associate Professor in the area of remote sensing and microwave technology. He has organized different invited sessions in international conferences on radar and SAR polarimetry. He has presented advanced courses and seminars on radar polarimetry to a wide range of organizations and events. His research interests include SAR and multidimensional SAR, radar polarimetry, physical parameter inversion, digital signal processing, estimation theory, and harmonic analysis.

Dr. López-Martínez is an Associate Editor of IEEE JOURNAL OF SELECTED TOPICS IN APPLIED EARTH OBSERVATIONS AND REMOTE SENSING and he served as Guest Editor of the European Association for Signal Processing (EURASIP), *Journal on Advances in Signal Processing*. He has Coauthored the paper awarded with the First Place Student Paper Award at the EUSAR 2012 Conference. He received the Student Prize Paper Award at the European Conference on Synthetic Aperture Radar (EUSAR) 2002 Conference.

Luca Pipia received the B.S. degree (*cum laude*) in electrical engineering from the Università Degli Studi di Cagliari, Cagliari, Italy, in 2002, and the Ph.D. degree in polarimetric differential SAR interferometry (PolDIInSAR) from the Universitat Politècnica de Catalunya (UPC), Barcelona, Spain, in 2009.

From June 2001 to December 2001, he was with the High-Frequency Institute of the German Aerospace Center (DLR), Oberpfaffenhofen, Germany, where he worked on land classification using polarimetric SAR (PolSAR) information. From 2003 to 2009, he was with the Remote Sensing Laboratory, Departament de Teoria del Senyal i Comunicacions, UPC, where he was deeply involved in the development and assessment of a novel polarimetric formulation of coherence-based advanced DinSAR techniques using real ground-based PolSAR data. Currently, he is with the Remote Sensing Group, Institut Cartogrà fic de Catalunya. His research interests include SAR polarimetry, differential SAR interferometry, and more recently, the retrieval of quantitative information from hyperspectral visible, near-, and thermal-infrared airborne data.

Dr. Pipia has served as a Reviewer for the IEEE JOURNAL OF SELECTED TOPICS IN APPLIED EARTH OBSERVATIONS AND REMOTE SENSING, the IEEE GEOSCIENCE AND REMOTE SENSING LETTERS, and the IEEE TRANSACTIONS ON GEOSCIENCE AND REMOTE SENSING.